# Surface electrostatics govern the emulsion stability of biomolecular condensates

Timothy J. Welsh[1,†], Georg Krainer[1,†], Jorge R. Espinosa[2,†], Jerelle A. Joseph[2], Akshay Sridhar[2], Marcus Jahnel[3,4,5], William E. Arter[1], Kadi L. Saar[1], Simon Alberti[4,*], Rosana Collepardo-Guevara[1,2,6*], Tuomas P.J. Knowles[1,2,*]

[1] Yusuf Hamied Department of Chemistry, University of Cambridge, Lensfield Road, Cambridge CB2 1EW, UK

[2] Cavendish Laboratory, University of Cambridge, J J Thomson Avenue, Cambridge CB3 0HE, UK

[3] Max Planck Institute of Molecular Cell Biology and Genetics, Pfotenhauerstr. 108, 01307 Dresden, Germany

[4] Biotechnology Center (BIOTEC), Center for Molecular and Cellular Bioengineering (CMCB), Technische Universität Dresden, Tatzberg 47/49, 01307 Dresden, Germany

[5] Cluster of Excellence "Physics of Life", TU Dresden, Dresden, Germany

[6] Department of Genetics, University of Cambridge, Cambridge CB2 3EH, UK

[†] These authors contributed equally to this work

* To whom correspondence may be addressed: Tuomas P.J. Knowles (tpjk2@cam.ac.uk), Rosana Collepardo-Guevara (rc597@cam.ac.uk), Simon Alberti (simon.alberti@tu-dresden.de)

**Abstract**

Liquid–liquid phase separation underlies the formation of biological condensates. Physically, such systems are microemulsions which in general have a propensity to fuse and coalesce; however, many condensates persist as independent droplets inside cells. This stability is crucial for their function, but the physicochemical mechanisms that control the emulsion stability of condensates remain poorly understood. Here, by combining single-condensate zeta potential measurements, optical microscopy, tweezer experiments, and multiscale molecular modelling, we investigate how the nanoscale forces that sustain condensates impact their stability against fusion. By comparing peptide–RNA ($PR_{25}$:PolyU) and proteinaceous (FUS) condensates, we show that a higher condensate surface charge correlates with a lower fusion propensity. Moreover, measurements of single condensate zeta potentials reveal that such systems can constitute classically stable emulsions. Taken together, these results highlight the role of passive stabilization mechanisms in protecting biomolecular condensates against coalescence.

**Keywords: liquid-liquid phase separation, microfluidics, zeta potential, colloid stability, FUS**

## Introduction

Solutions of multivalent macromolecules, especially disordered proteins and nucleic acids, have the ability to undergo demixing through liquid–liquid phase separation (LLPS) (*1*, *2*). LLPS enables the formation of condensed liquid droplets, which coexist with a dilute aqueous phase (*3–5*). In living cells, LLPS has been shown to underlie the formation of biomolecular condensates, which function as membraneless organelles. This process provides a mechanism for the spatiotemporal control (*6*) of several vital processes (*7*), including RNA processing and stress signaling (*8, 9*). Moreover, aberrant LLPS, often involving liquid-to-solid transitions, has been implicated in the emergence of various neuropathologies, age-related diseases, and cancer (*10–12*).

Biomolecular condensates are highly diverse systems, both in terms of composition, size, and behavior. Not only is the range of different proteins and nucleic acids that can undergo LLPS both *in vitro* and in cells vast (*8*, *10*, *13*), but mounting evidence also suggests that the detailed chemical nature of the interactions that drive these diverse systems to phase separate spans a range of charge–charge, cation–π, π–π, polar, hydrophobic, and even hybrid interactions (*2*, *14*, *15*). A unifying feature of intracellular LLPS is that, in most if not all cases, condensate formation is driven by a combination of both electrostatic and non-ionic interactions; the balance of these forces is determined by the molecular nature and surrounding microenvironment (*15*).

In addition, biomolecular condensates exhibit a significant variation in their fusion and coalescence propensities, with broad functional implications (*16–18*). For instance, processes like stress adaptation and signaling (*7, 19*) depend on the ability of phase-separated liquid drops to remain stable against fusion for varying periods of time that range from seconds to hours. In other cases, such as the nucleoli, fusion of droplets into a single condensate phase may be critical for clustering of RNA and subsequent functionality (*20*). Previous work has suggested that active chemical and biological processes in cells may operate to prevent droplet coalescence (*21*). Observations of liquid condensates coexisting *in vitro* without undergoing fusion also suggest that passive mechanisms exist which prevent condensates from fusing and clustering (*22–24*). These examples motivate the question to what extent passive forces might sustain condensate stability and impact their propensity to coalesce or to remain stable against fusion in the cell.

Physically, biomolecular condensates are water-in-water emulsions with a very low surface tension, similar to other polyelectrolyte coacervates or colloidal assemblies (*21*). A specific quantity of

interest to describe the stability of such emulsions against coalescence, coagulation, and clustering is their zeta potential (*25–27*)—the electrical potential at the edge of the interfacial double layer of ions and counter-ions near the surface of any charged particle (Figure 1A) (*28, 29*). Low absolute values of the zeta potential, typically smaller than 30 or 40 mV depending on the nature of the molecules making up the emulsions, tend to be associated with unstable emulsions constituted from droplets that fuse (*30, 31*), while high absolute values of the potential result in stability against fusion (*32*, *33*). Based on these observations, we sought to examine if the zeta potential of protein condensates, as a passive stabilization mechanism, could be established as a parameter to assess and predict the propensity of condensates to fuse and coalesce spontaneously, and to infer electrostatic properties of condensate surfaces. Moreover, we aimed to rationalize how mesoscale zeta potential values emerge from the distribution and molecular organization of proteins, water, and ions in and around condensates.

To this end, we devised a microfluidic approach that enables measurement of zeta potentials at the resolution of individual condensates. We correlated these measurements with the propensity of condensates to fuse and coalesce using light microscopy, as well as optical tweezer experiments. To further enlighten our molecular understanding of the experimental observations, we developed a multiscale molecular modelling strategy that equilibrates protein condensates at coarse-grained resolution and then back-maps them to the atomistic level. We show that zeta potentials obtained for a range of biomolecular condensates, including a dipeptide proline–arginine condensate system ($PR_{25}$) phase separated with polyuridine (PolyU) and the protein fused in sarcoma (FUS) including a pathogenic variant, correlate well with their propensity to fuse, coalesce, and cluster, as observed by light microscopy and tweezer experiments. Our multiscale molecular dynamics simulations link these fusion propensities to the modulation of the surface tension of condensates via surface electrostatics. These results establish the zeta potential as a fundamental quantity to infer the tendency of biomolecular condensates to fuse and coalesce and rationalize it from the molecular organization of charged species in the system.

## Results and Discussion

**Single-condensate zeta potential measurements.** To quantify the zeta potential of biomolecular condensates experimentally, we developed a single-particle microfluidic approach based on free-flow electrophoresis (μFFE) using a 3D device, that enables in-solution quantification of zeta potentials with single-droplet resolution (Figure 1B–D). μFFE has been previously used for the measurement of protein charge (*34*, *35*) and the separation of proteins and nucleic acids (*36*). The experimental approach is

illustrated in Figure 1B–D. In short, condensates are subjected to an electric field perpendicular to their flow and from their displacement velocity we obtain their electrophoretic mobility which is correlated with zeta potential (Figure 1C) (additional description in Supporting Information). In this manner, zeta potential distributions from measurements of thousands of individual condensates may be obtained within a few minutes (Figure 1D). This approach provides the high resolution which is especially important for samples that are poly-dispersed both in zeta potential and size, as is the case for liquid biomolecular condensates.

Using our method, zeta potentials were acquired for three different biomolecular condensates. We first focused on a dipeptide repeat derived from the hexanucleotide repeat expansion in the chromosome 9 open reading frame 72 (*C9orf72*), implicated in amyotrophic lateral sclerosis (ALS) (*37*, *38*). The peptide used consisted of 25 repeats of the dipeptide proline-arginine ($PR_{25}$). This type of peptide is well known to phase separate when mixed with negatively charged polymers (*4*, *38*), including single-stranded RNA consisting of 2500–3500 bases of uridine (PolyU). Additionally, the protein fused in sarcoma (FUS) was studied. FUS is a widely expressed RNA-binding protein that has been shown to phase separate and has been correlated with ALS phenotypes, it is especially toxic when it forms aggregates in the absence of RNA (*39–41*). We also studied the disease related mutant FUS G156E, which is known to have a faster transition from the liquid-condensed state to the solid state (*10*). Both FUS variants were expressed with a C-terminal EGFP fluorescent protein tag for visualization purposes. The proteins and the peptide:RNA system typify two distinct classes of condensates: those formed via homotypic interactions (*e.g.*, multivalent interactions between the disordered regions and domains of FUS (*42*)), and those sustained by heterotypic interactions (*e.g.*, the association of polyanions and polycations in the $PR_{25}$:PolyU system through complex coacervation (*43*)).

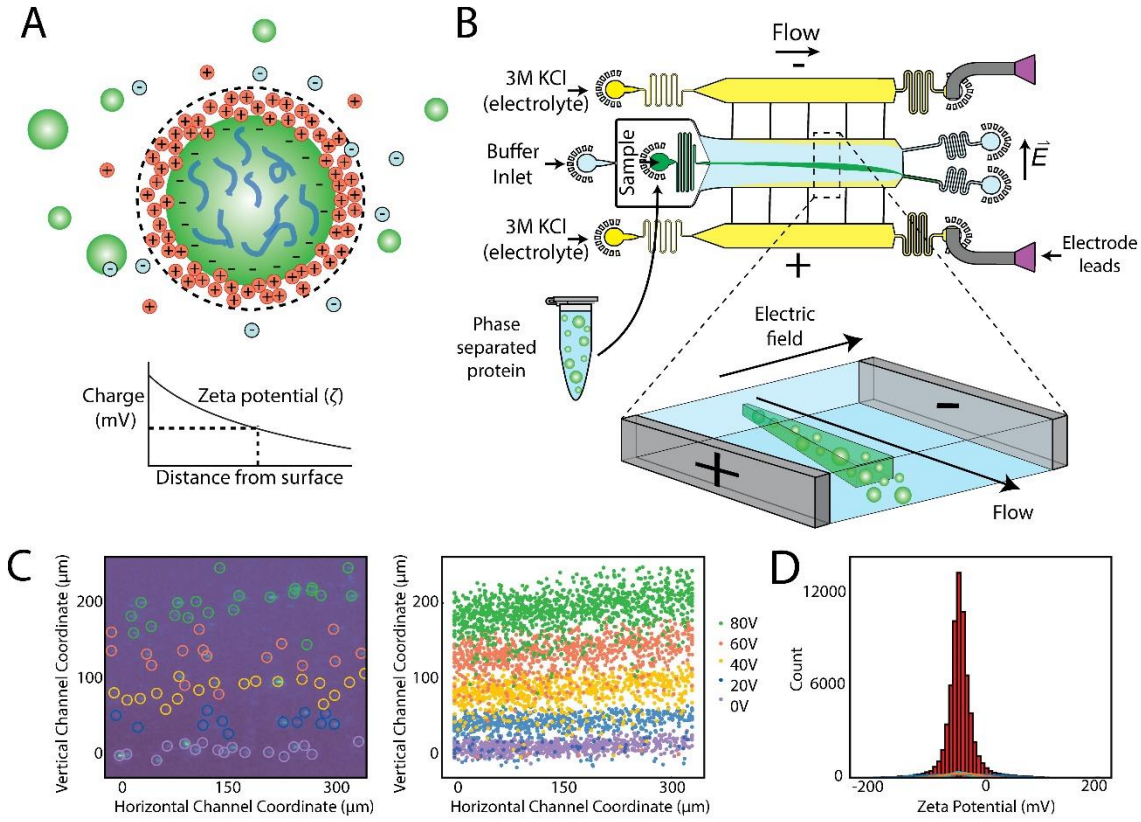


**Figure 1. Overview of the microfluidic platform for quantifying single-condensate zeta potentials. (A)** Schematic of the zeta potential of a protein condensate, which is the electrical potential at the edge of the ion layer surrounding a particle, denoted by the dashed lines. **(B)** Schematics of the µFFE device used to carry out the single-droplet zeta potential measurements. Phase separated droplets were introduced into the 3D free-flow electrophoresis device through a central injection port, preventing any contact between the condensates and the surface of the channel. The condensates were then deflected by applying a constant voltage and positions quantified as a measure of electrophoretic mobility to calculate zeta potentials. **(C)** Left panel: Overlaid images from multiple voltage applications in the range from 0–80 V, depicting individual protein condensates as they move through the image frame. Right panel: Tracked coordinates of detected condensates at each voltage in the range between 0 and 80 V; these coordinates were used to calculate the zeta potential (see Supporting Materials and Methods). **(D)** Each individual condensate was analyzed to yield single-condensate zeta potential distributions, represented as the sum of all obtained measurements across all voltages applied. Cityscapes at the bottom of each filled histogram are histograms derived from single voltage measurement.

Each of the phase separating systems was assessed using µFFE to determine zeta potential distributions from thousands of individually probed biomolecular condensates. Figure 2A-C shows the range of zeta potentials obtained across the different protein condensates, as given by their mean values ($\mu$), and their degree of heterogeneity, as assessed by the standard deviation of the distributions ($\sigma$). The trend of absolute zeta potentials of the condensates from largest to smallest was $PR_{25}$:PolyU > FUS wild type > FUS G156E, with mean zeta potential values ranging from –40.6 mV to –15.0 mV. The distributions also showed that the condensates are poly-dispersed in zeta potential, as evidenced by the

tails of the distribution. Further analysis revealed that the condensate systems are poly-disperse in size; yet there is no distinct correlation between zeta potential and size (Figure S3).

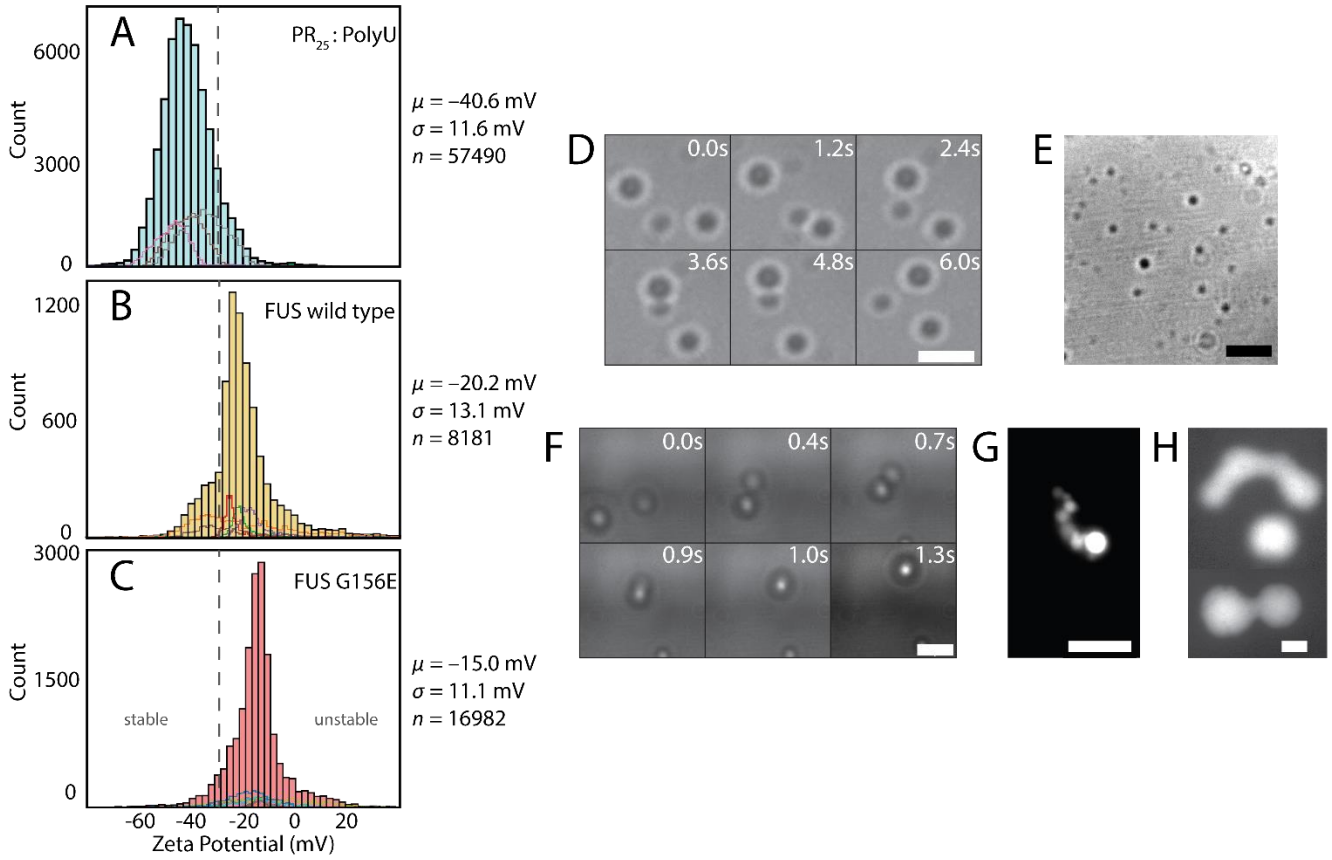


**Figure 2. Single-droplet zeta potential measurements of biomolecular condensates and observations of condensate stability from epifluorescence and phase-contrast microscopy.** Histograms of single condensate zeta potential measurements for **(A)** $PR_{25}$:PolyU, **(B)** FUS wild type, and **(C)** FUS G156E condensates. Histograms were obtained from all measurements taken on a particular condensate system across all voltages applied, as illustrated in Figure 1. Solid line distributions in each panel at the bottom of each filled histogram represent a collection of measurements from a single replicate at a particular voltage value, while the larger filled distribution represents the sum of >5 replicates of each system. Mean, $\mu$, and width, $\sigma$, of distributions as well as number of droplets, $n$, probed are given. Dashed lines indicate boundaries for stable and unstable dispersion with zeta potential cut-offs at –30 mV (*25*, *31*). **(D, E)** Images of $PR_{25}$:PolyU condensates from phase contrast microscopy, **(F, G)** FUS wild-type condensates from phase contrast and epifluorescence microscopy, and **(H)** FUS G156E condensates from epifluorescence microscopy. All scale bars are 3 μm.

**Correlating condensate zeta potential with fusion propensity.** Since zeta potential is a key parameter in determining the passive stability of emulsions against droplet coalescence or fusion and clustering (*27*, *32*), we next assessed the fusion propensity of $PR_{25}$:PolyU and FUS condensates by monitoring droplets merging using light microscopy (*9*, *38*). We observed that $PR_{25}$:PolyU condensates remain stable against

fusion (Figure 2D,E), as has been previously reported (*38*) while FUS wild type condensates rapidly fuse and cluster within seconds to minutes after mixing (Figure 2F,G), in line with previous observations (*10*). Similarly, FUS G156E condensates rapidly fuse together within minutes after phase separation (Figure 2H). These observations indeed support a correlation between zeta potential and a barrier to condensate fusion.

We further investigated the fusion propensities using dual-trap optical tweezers (*10, 14*) (Figure 3). In these experiments on our two test systems, $PR_{25}$:PolyU condensates showed a higher resistance against fusion compared to FUS wild type condensates. Whereas FUS condensates fused immediately upon contact, $PR_{25}$:PolyU condensates required an additional force to initiate a fusion event, indicating the presence of a repulsion between the condensates. This characteristic is evident in images of moderately deformed $PR_{25}$:PolyU droplets just before fusion, and a dip in force measurements from optical tweezer experiments suggesting an increased repulsive force (Figure 3A). This repulsion was absent in FUS condensates. These observations correlate well with the findings that $PR_{25}$:PolyU condensates have a greater absolute zeta potential compared to FUS, and thus show that a greater absolute zeta potential indeed correlates with an increased barrier to fusion. Interestingly, although there seems to be a higher energy barrier to initiate droplet fusion in $PR_{25}$:PolyU condensates (Figure 3B, bottom panel), once started, fusion proceeds much faster for $PR_{25}$:PolyU condensates than for FUS wild-type condensates (Figure 3B, top panel), suggesting that there is no correlation between the barrier to fusion and the fusion rate. These findings also show that both condensate systems tested are able to fuse and relax back to spherical structures, supporting that these are both liquid condensate systems whose fusion propensities are dictated by the surface features and not necessarily by their viscoelastic properties, as is the case for condensates in other conditions (*10*, *44*).

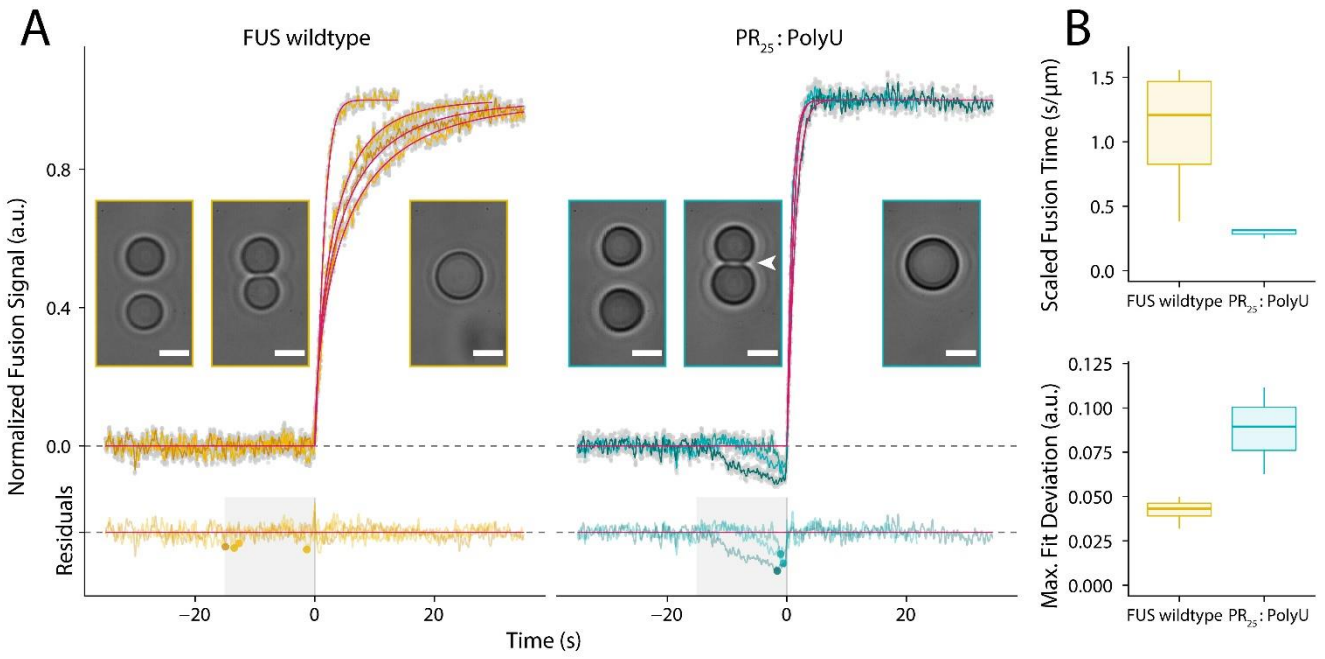


**Figure 3. Assessment of condensate stability in controlled coalescence experiments by optical tweezer measurements**. **(A)** Example traces of controlled droplet fusions using optical tweezers of FUS wild-type and $PR_{25}$:PolyU droplets, together with model fits (magenta) and corresponding residuals. Raw data for individual fusion events are shown as grey points and smoothed signals as colored lines. Only 5% of the raw data is displayed for visualization purposes. For each condition, representative images before fusion, at the onset of fusion, and after fusion are shown. $PR_{25}$:PolyU droplets exhibited a clear indentation (white arrow) before fusion is initiated. All scale bars are 3 µm.. A significant deviation from the standard fusion model, as illustrated by the dip in the residuals, reflects an energy barrier to be overcome to induce $PR_{25}$:PolyU droplet fusion. We used a window of 15 seconds before fusion onset to quantify the maximum deviation from the model (colored data points). **(B)** Top panel: Size normalized relaxation times indicate that once initiated, $PR_{25}$:PolyU droplets fuse faster than FUS wild-type droplets. Bottom panel: Maximum deviation from the standard model serves as a proxy for the repulsive force required to start fusion.

**Multiscale molecular simulations.** To understand the molecular origin of the measured zeta potential values and explore correlations with variations in the molecular organization within condensates, in particular the spatial distribution of charged amino acids and the concentration of ions within, we developed a multiscale molecular simulation approach (Figure 4). We started by using a reparameterization of the sequence-dependent LLPS coarse-grained (CG) model of the Mittal group (*45–47*) to simulate the formation of full length FUS and $PR_{25}$:PolyU condensates by means of Direct Coexistence (DC) simulations (*48–50*) of tens to hundreds of interacting biomolecules (Figure 4; Step 1; further details on the DC technique and on the employed CG model are provided in the Computational Section of the Supporting Information). Our method back-maps equilibrium coarse-grained condensates to fully atomistic systems, including explicit solvent and ions (Figure 4; Steps 2–4), and investigates differences in the absorption and distribution of ions between the condensed and dilute phase in both

systems (Figure 5). Such a multiscale procedure (Figure 4) is necessary to capture explicit all-atom descriptions of biomolecules, water, and ions, while keeping the model feasible for computation given the large system and long timescales.

Back-mapping coarse-grained protein condensates into all-atom configurations is not a trivial task since it requires expanding the single bead position for each protein residue (from CG simulations) to atomistic-level amino acids that preserve geometric and environmental conditions without displaying particle overlapping. Our multiscale approach breaks the problem down into three steps (Figure 4; Steps 2–4). Each step utilizes standard and widely available biomolecular modelling tools, making our overall procedure easily implementable and fully transferable to other condensed-phase protein systems as explained in Figure 4.

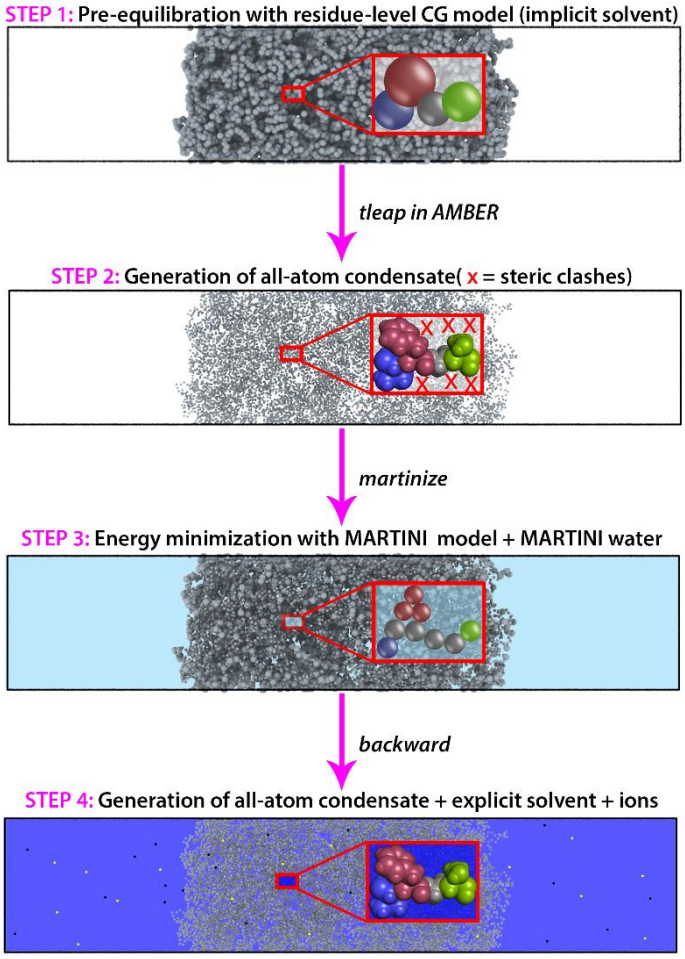


**Figure 4. Multiscale strategy for generation of all-atom condensates from pre-equilibrated high-resolution coarse-grained simulations**. ***Step 1***: The system is first equilibrated at residue-level resolution using a reparameterization of the Mittal group coarse-grained model (*46*, *47*). ***Step 2***: The coarse-grained bead coordinates are unwrapped across the periodic boundaries and unwrapped bead positions are defined as coordinates for the amino-acid Cα atoms. Using the tleap module of

Amber16 (*51*), missing sidechain and backbone atoms are added in random orientations. ***Step 3***: Because adding atoms in this way results in significant atomic overlaps that cannot be resolved via standard energy minimization procedures. To dispose of the steric clashes, atomistic configurations are mapped to the higher-resolution coarse grained model Martini (*52*) and standard Martini Water (*53*). The system's energy was then minimized. This third step is key to make our approach applicable not only to intrinsically disordered peptides like $PR_{25}$, but also to large multidomain proteins with globular regions, like FUS. ***Step 4***: Finally, the program "backward" (*54*) was used to back-map the Martini configuration to the full atomistic resolution (see further details in the Supporting Information).

**Insights into the molecular organization of condensates.** Our multiscale simulations reveal that both $PR_{25}$:PolyU and FUS condensates (Figure 5A,B) exhibit a mostly homogeneous distribution of charged and uncharged species at physiological salt (Figure 5C). This is not surprising for $PR_{25}$:PolyU condensates which are mostly sustained by electrostatic interactions (Arg:U). Indeed, we find a uniform distribution of all species (U, Pro, Arg) at the core of the $PR_{25}$:PolyU condensates (Figure 5; $PR_{25}$:PolyU). More surprisingly, a mostly homogenous molecular organization for FUS condensates is remarkable given the complexity of the FUS sequence (see Supporting Material). The 526-residue FUS polypeptide chain can be partitioned into an uncharged disordered prion-like domains (*55*) (PLD) enriched in Gln, Gly, Ser, and Tyr (residues 1–165), three positively charged disordered Arg-Gly-Gly (RGG) rich regions (RGG1: residues 166–267, RGG2: residues 371–421, and RGG3: residues 454–526), and two globular regions (a RNA-recognition motif: residues 282–371, and a zinc finger: residues 422–453) (*56*). In agreement with experiments (*14*, *57*, *58*), we find that FUS condensates are most strongly stabilized by interdomain interactions both electrostatic (RGG1/3–PLD) and hydrophobic (PLD–PLD) in nature (Figure S5). These preferential patterns of interactions among FUS regions/domains result in homogeneous condensates in the probed conditions.

A crucial difference between the molecular organization of FUS and $PR_{25}$:PolyU condensates is the much higher concentration of charged species (both positive and negative) in $PR_{25}$:PolyU condensates versus FUS, including those at the condensate surfaces (Figure 5C and 5E, and Figure S6). Although the core of $PR_{25}$:PolyU condensates have a homogeneous distribution of positive and negative molecules, the surface itself is more concentrated in $PR_{25}$ peptides (Figure S7), and hence is rich in positive charge. When measuring the interfacial free energy of the condensates in our simulations, we find that its value for FUS condensates ($0.35\pm4$ mJ/m$^2$) is almost twice of that for $PR_{25}$:PolyU droplets ($0.20\pm 4$ mJ/m$^2$), supporting the trend that condensates which concentrate more charged species (*e.g.*, positively charged $PR_{25}$ tails) at the surface (Figure S7) tend to have lower interfacial free energies. This surface geometry would also result in higher electrostatic repulsion and higher surface charge—in agreement with the experimental observations of higher zeta potentials for $PR_{25}$:PolyU compared to FUS. Nevertheless, we note that even

though highly charged interfaces exhibiting large absolute zeta potential values (as those found in $PR_{25}$:PolyU droplets) can typically present low interfacial free energies, not every condensate with low interfacial free energy would necessarily display analogously large absolute zeta potential values. For instance, multilayer complex coacervates coated by surfactant proteins that preferentially locate at droplet surfaces can be uncharged and still reduce significantly the interfacial free energy—due to surfactant proteins having effective lower valencies than those of the core-located scaffold proteins—while displaying presumably low zeta potential values due to their uncharged nature (*24*, *59*, *60*).

Besides a higher density of charged species (Figure 5B,C; left), $PR_{25}$:PolyU condensates establish more favorable electrostatic interactions with counterions than FUS condensates. The high concentration of charge at $PR_{25}$:PolyU surfaces is evident from the higher density of counterions at the interface than at the condensate core, and most notable of $Cl^-$ ions, which are needed to screen the solvent-exposed $PR_{25}$ tails. In agreement, FUS condensates, which contain less charged amino acids overall (Figure 5B,C; right), also absorb a lower total concentration of counterions.

As expected, our simulations reveal that counterions have smaller diffusion coefficients within the condensed phase, where they can bind to other charged species (*61*). Interestingly, counterions diffuse more slowly within FUS condensates than within $PR_{25}$:PolyU condensates (Table S1). This observation likely stems from the higher molecular density of FUS condensates (~0.54 g/cm$^3$) versus $PR_{25}$:PolyU condensates (~0.40 g/cm$^3$), the abundance of Arg residues in FUS available to establish strong cation-anion interactions with $Cl^-$, and the lack of other negatively charged species to displace $Cl^-$ from their FUS absorption sites. Consistently, in the more charge-rich $PR_{25}$:PolyU condensates, counterions diffuse slightly more freely because of the lower condensate density, and since Arg and U are already paired up and establish strong cation–anion interactions (Table S1).

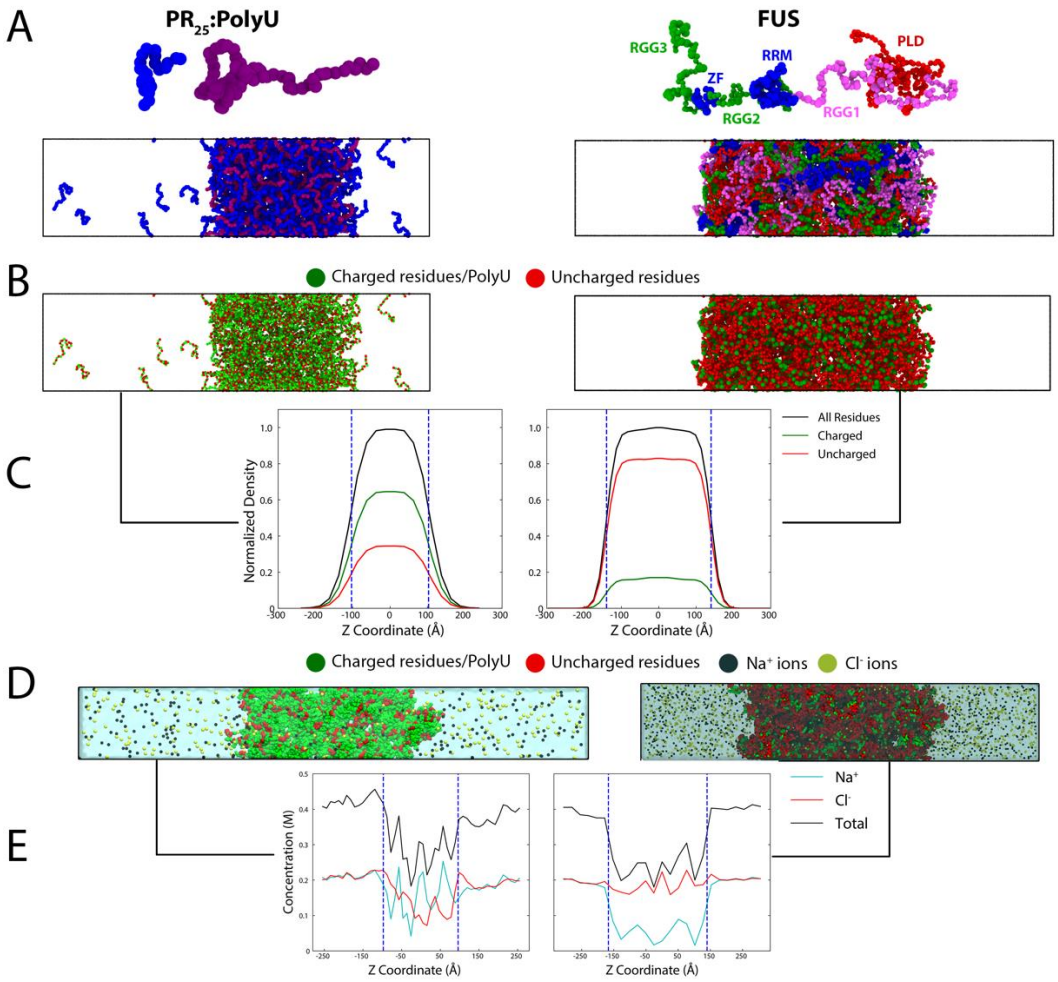


**Figure 5. Molecular organization of $PR_{25}$:PolyU and FUS condensates. (A)** Top panel: One-bead per amino acid/nucleotide coarse-grained representation of $PR_{25}$ (blue), PolyU (purple) and FUS with the PLD (residues 1–165) in red, the extended arginine rich region 1 (RGG1; residues 166–284) in pink, the RNA-recognition motif (RRM; residues 285–371) and the Zinc Finger region (ZF; residues 423–453) in blue, the arginine rich regions 2 (RGG2; residues 372–422) and 3 (RGG3; residues 454–526) in green. Bottom panel: Representative coarse-grained equilibrium configurations obtained via direct coexistence simulations (*i.e.*, both liquid phases simulated in the same simulation box) of (left) $PR_{25}$:PolyU and (right) FUS condensates. **(B)** Representative configurations from A but with charged species (amino acids and PolyU) colored green and uncharged residues colored red. **(C)** Normalized density of charged and uncharged species across the long side of the simulation box estimated over the coarse-grained equilibrium ensemble showing a much higher concentration of charge in $PR_{25}$:PolyU. The vertical dashed lines show the location of the edge of the condensate. **(D)** Back-mapped atomistic system from equilibrium coarse-grained configurations used to estimate the differential behavior of ions in $PR_{25}$:PolyU and FUS condensates. **(E)** Ion distributions in $PR_{25}$:PolyU and FUS condensates estimated from atomistic direct coexistence molecular dynamics simulations. The vertical dashed lines indicate the approximate locations of the condensate interfaces (condensates are positioned in the center and are in contact with a surrounding diluted phase). The simulations were prepared ensuring similar equilibrium concentrations of ions in the diluted phases of both systems.

Collectively, our simulation results and experimental zeta potential measurements suggest that larger absolute zeta potential values occur in systems that are more highly charged overall, and,

importantly, that exhibit a higher total charge at the surface, where continuous dynamical reconstruction of the interfacial structure occurs via capillary wave fluctuations (*62*, *63*).

**Conclusion**

In this work, we have explored the role of passive electrostatic mechanisms on the emulsion stability of biomolecular condensates. By measuring the zeta potential on a single condensate level, we probed the electrostatic forces between individual biomolecular condensates of $PR_{25}$:PolyU and FUS and correlated these experimental results with their observed stability against fusion. A larger absolute value of condensate zeta potential confers greater resistance against coalescence and clustering in a manner which is analogous to oil-in-water emulsions (*30–32*). Additionally, the wide distributions in zeta potentials indicate that a population of condensates is likely to have varying degrees of fusion propensities within it, and that condensates are highly diverse in surface composition.

Our multiscale molecular modelling approach further described the detailed molecular behavior of these condensates, including their surface charge density and its impact on their interfacial free energy, the intermolecular interactions of the component biomolecules, and the distribution and mobility of ions in- and outside of condensates. These simulations explain the observed difference in zeta potential values and droplet fusion rates through a molecular characterization of the charge distribution within the condensates, both in the core and the surfaces, and through the evaluation of the interfacial free energy. While $PR_{25}$:PolyU condensates are stabilized mostly by electrostatic interactions and possess highly positively-charged surfaces, FUS droplets are predominantly sustained by cation–π and hydrophobic interactions, and exhibit only modestly charged interfaces. These findings, therefore, establish the surface charge density of condensates as the molecular origin of the modulation of their propensity to fuse, and the zeta potential as a fundamental quantity to infer it. Moreover, the analysis of the NaCl ion distribution and their mean square displacement along the condensates provides a fundamental description of the electrostatic interaction strength contributing to the random and dynamical percolated network (*64*) sustaining the stability of these biomolecular condensates.

The correlation between electrostatic properties and condensate stability against fusion, as predicted by classical emulsion theory, may be of significance for the modulation of condensate stability in cells. In addition to the known active chemical and biological processes that modulate condensate stability (*21*, *65*) ,our work suggests that also passive mechanisms exist which prevent condensates from fusing and clustering. Such passive stabilization stems from a combination of repulsive forces between

condensates, and the effects that surface electrostatics have on lowering the surface tension of the droplets. Likewise, cells may actively control the stability of condensates by tuning the condensate surface charge, (*e.g.* by tuning factors like temperature, pH, and ion concentration gradients, all of which influence LLPS behavior (*21*, *66*)).

The observed correlation between emulsion stability and zeta potential also has important implications for diseases, specifically for liquid-to-solid transitions of the condensates. It has been shown that FUS can transition into toxic aggregates associated with the onset and development of motor neuron disease more readily when it is contained in condensates (*10*), and this trend holds true for other proteins as well, including TDP-43 and other condensate forming systems (*67*, *68*). Recent theoretical work has highlighted how condensates could behave as compartments for aggregate formation, and has also indicated how more aggregates could form within condensates of greater size (*69*). Since zeta potential may have a direct effect on condensate fusion and size, it is possible that lower zeta potential condensates will fuse into bigger condensates for potential aggregate nucleation. Beyond pathophysiological implications, the immiscibility and size control of phase separated condensates has been indicated to be relevant particularly in the control of the size of organelles during cell growth and embryonic development (*70*, *71*). Additionally, the size of condensates could be a marker of cancer proliferation (*72*), suggesting that the modulation of the size of certain condensates, controlled through their zeta potential, could be exploited for therapeutic interventions.

Overall, our work shows how classical colloid physics properties, such as the zeta potential and emulsion stability, can contribute to the stabilization of biomolecular condensates. These findings expand our understanding of the physical and molecular factors that control the emulsion stability of condensates, and may have implications in the study of the roles of biomolecular condensates in health and disease.

**Associated content**

**Supporting Information.** Methods and Supporting Methods, Supporting Results, Supporting Computational Methods, Supporting Figures: Figure S1. Full schematic of μFFE device; Figure S2. Electrical circuit and calibration of device; Figure S3. Size dependence of zeta potential; Figure S4. Zeta potential measurement of 60 nm gold nanoparticles; Figure S5. Contacts between FUS domains in condensates; Figure S6. Density of charged atoms in $PR_{25}$:PolyU and FUS condensates; Figure S7. Structure of $PR_{25}$:PolyU condensates; Supporting Table: Table S1. Diffusion rates and mobility ratios of ions in condensates.

## Author Information

**Author contributions.** T.J.W., G.K., and T.P.J.K. conceived of the idea and designed research. T.J.W. carried out all microfluidic experiments and analyzed the data. J.R.E., J.A.J., A.S., and R.C.G. designed the simulations. J.R.E. and J.A.J. performed the coarse-grained simulations. A.S. performed the atomistic simulations. J.R.E., J.A.J., and A.S. analyzed the simulation results. M.J., T.J.W., and G.K. performed and analyzed optical tweezer experiments. R.C.G. supervised the simulation work. W.E.A. and K.L.S. provided microfluidics chip designs and data analysis approaches. S.A. provided protein materials. T.J.W., G.K., J.RE, R.C.G. and J.A.J. wrote the manuscript. All authors edited the manuscript.

**Notes.** The authors declare no competing financial interest

## Acknowledgments

We thank members of the Knowles laboratory for discussions. We thank Jeetain Mittal and Gregory L. Dignon for invaluable help with the implementation of their sequence-dependent protein coarse-grained model in LAMMPS. The research leading to these results has received funding from the European Research Council (ERC) under the European Union's Seventh Framework Programme (FP7/2007-2013) through the ERC grant PhysProt (agreement no. 337969) (T.P.J.K.), under the European Union's Horizon 2020 Framework Programme through the Future and Emerging Technologies (FET) grant NanoPhlow (agreement no. 766972) (T.P.J.K., G.K.), under the European Union's Horizon 2020 Framework Programme through the Marie Sklodowska-Curie grant MicroSPARK (agreement no. 841466) (G.K.), and under the European Union's Horizon 2020 research and innovation programme through the ERC grant InsideChromatin (agreement no. 803326) (R.C.G.). We further thank the Newman Foundation (T.P.J.K.), the Biotechnology and Biological Sciences Research Council (T.P.J.K.), the Herchel Smith Funds of the University of Cambridge (G.K.), the Wolfson College Junior Research Fellowship (G.K.), the Winston Churchill Foundation of the United States (T.J.W.), the Harding Distinguished Postgraduate Scholar Programme (T.J.W.), the Winton Advanced Research Fellowship (R.C.G.), the Oppenheimer Research Fellowship (J.R.E.), the Roger Ekins Fellowship (J.R.E.), the King’s College Research Fellowship (J.A.J.), the Engineering and Physical Sciences Research Council (K.L.S.), and the Schmidt Science Fellowship program in partnership with the Rhodes Trust (K.L.S.). The simulations were performed using resources provided by the Cambridge Tier-2 system operated by the University of Cambridge Research Computing Service (http://www.hpc.cam.ac.uk) funded by EPSRC Tier-2 capital grant EP/P020259/1.

## References


1. P. Li, S. Banjade, H. C. Cheng, S. Kim, B. Chen, L. Guo, M. Llaguno, J. V. Hollingsworth, D. S. King, S. F. Banani, P. S. Russo, Q. X. Jiang, B. T. Nixon, M. K. Rosen, Phase transitions in the assembly of multivalent signalling proteins. *Nature*. **483**, 336–340 (2012).

2. E. W. Martin, A. S. Holehouse, I. Peran, M. Farag, J. J. Incicco, A. Bremer, C. R. Grace, A. Soranno, R. V. Pappu, T. Mittag, Valence and patterning of aromatic residues determine the phase behavior of prion-like domains. *Science*. **367**, 694–699 (2020).

3. S. Alberti, A. Gladfelter, T. Mittag, Considerations and Challenges in Studying Liquid-Liquid Phase Separation and Biomolecular Condensates. *Cell*. **176**, 419–434 (2019).

4. S. Boeynaems, S. Alberti, N. L. Fawzi, T. Mittag, M. Polymenidou, F. Rousseau, J. Schymkowitz, J. Shorter, B. Wolozin, L. Van Den Bosch, P. Tompa, M. Fuxreiter, Protein Phase Separation: A New Phase in Cell Biology. *Trends Cell Biol.* **28**, 420–435 (2018).

5. A. A. Hyman, C. A. Weber, F. Jülicher, Liquid-Liquid Phase Separation in Biology. *Annu. Rev. Cell Dev. Biol.* **30**, 39–58 (2014).

6. C. F. Lee, C. P. Brangwynne, J. Gharakhani, A. A. Hyman, F. Jülicher, Spatial Organization of the Cell Cytoplasm by Position-Dependent Phase Separation. *Phys. Rev. Lett.* **111**, 088101 (2013).

7. J. A. Riback, C. D. Katanski, J. L. Kear-scott, V. Evgeny, A. E. Rojek, T. R. Sosnick, D. A. Drummond, Tuned Response. *Cell*. **168**, 1028–1040 (2018).

8. M. Feric, N. Vaidya, T. S. Harmon, D. M. Mitrea, L. Zhu, T. M. Richardson, R. W. Kriwacki, R. V. Pappu, C. P. Brangwynne, Coexisting Liquid Phases Underlie Nucleolar Subcompartments. *Cell*. **165**, 1686–1697 (2016).

9. C. P. Brangwynne, C. R. Eckmann, D. S. Courson, A. Rybarska, C. Hoege, J. Gharakhani, F. Jülicher, A. A. Hyman, Germline P Granules Are Liquid Droplets That Localize by Controlled Dissolution/Condensation. *Science*. **324**, 1729–1732 (2009).

10. A. Patel, H. O. Lee, L. Jawerth, S. Maharana, M. Jahnel, M. Y. Hein, S. Stoynov, J. Mahamid, S. Saha, T. M. Franzmann, A. Pozniakovski, I. Poser, N. Maghelli, L. A. Royer, M. Weigert, E. W. Myers, S. Grill, D. Drechsel, A. A. Hyman, S. Alberti, A Liquid-to-Solid Phase Transition of the

ALS Protein FUS Accelerated by Disease Mutation. *Cell*. **162**, 1066–1077 (2015).

11. S. Alberti, S. Carra, Quality Control of Membraneless Organelles. *J. Mol. Biol.* **430**, 4711–4729 (2018).

12. S. Alberti, A. A. Hyman, Are aberrant phase transitions a driver of cellular aging? *BioEssays*. **38**, 959–968 (2016).

13. T. M. Franzmann, M. Jahnel, A. Pozniakovsky, J. Mahamid, A. S. Holehouse, E. Nüske, D. Richter, W. Baumeister, S. W. Grill, R. V. Pappu, A. A. Hyman, S. Alberti, Phase separation of a yeast prion protein promotes cellular fitness. *Science*. **359**, eaao5654 (2018).

14. J. Wang, J. M. Choi, A. S. Holehouse, H. O. Lee, X. Zhang, M. Jahnel, S. Maharana, R. Lemaitre, A. Pozniakovsky, D. Drechsel, I. Poser, R. V. Pappu, S. Alberti, A. A. Hyman, A Molecular Grammar Governing the Driving Forces for Phase Separation of Prion-like RNA Binding Proteins. *Cell*. **174**, 688–699 (2018).

15. G. Krainer, T. J. Welsh, J. A. Joseph, J. R. Espinosa, S. Wittmann, E. de Csilléry, A. Sridhar, Z. Toprakcioglu, G. Gudiškytė, M. A. Czekalska, W. E. Arter, J. Guillén-Boixet, T. M. Franzmann, S. Qamar, P. S. George-Hyslop, A. A. Hyman, R. Collepardo-Guevara, S. Alberti, T. P. J. Knowles, Reentrant liquid condensate phase of proteins is stabilized by hydrophobic and non-ionic interactions. *Nat. Commun.* **12** (2021), doi:10.1038/s41467-021-21181-9.

16. S. Elbaum-Garfinkle, Y. Kim, K. Szczepaniak, C. C. H. Chen, C. R. Eckmann, S. Myong, C. P. Brangwynne, The disordered P granule protein LAF-1 drives phase separation into droplets with tunable viscosity and dynamics. *Proc. Natl. Acad. Sci. U. S. A.* **112**, 7189–7194 (2015).

17. J. R. Wheeler, T. Matheny, S. Jain, R. Abrisch, R. Parker, Distinct stages in stress granule assembly and disassembly. *Elife*. **5**, e18413 (2016).

18. J. D. Wurtz, C. F. Lee, Chemical-Reaction-Controlled Phase Separated Drops: Formation, Size Selection, and Coarsening. *Phys. Rev. Lett.* **120**, 078102 (2018).

19. X. Su, J. A. Ditlev, E. Hui, W. Xing, S. Banjade, J. Okrut, D. S. King, J. Taunton, M. K. Rosen, R. D. Vale, Phase separation of signaling molecules promotes T cell receptor signal transduction. *Science*. **352**, 595–599 (2016).

20. M. Feric, C. P. Brangwynne, A nuclear F-actin scaffold stabilizes ribonucleoprotein droplets

against gravity in large cells. *Nat. Cell Biol.* **15**, 1253–1259 (2013).

21. C. A. Weber, D. Zwicker, F. Jülicher, C. F. Lee, Physics of active emulsions. *Reports Prog. Phys.* **82**, 064601 (2019).

22. A. Molliex, J. Temirov, J. Lee, M. Coughlin, A. P. Kanagaraj, H. J. Kim, T. Mittag, J. P. Taylor, Phase Separation by Low Complexity Domains Promotes Stress Granule Assembly and Drives Pathological Fibrillization. *Cell*. **163**, 123–133 (2015).

23. J. Berry, C. P. Brangwynne, M. Haataja, Physical principles of intracellular organization via active and passive phase transitions. *Reports Prog. Phys.* **81**, 046601 (2018).

24. I. Sanchez-Burgos, J. A. Joseph, R. Collepardo-Guevara, J. R. Espinosa, Size conservation emerges spontaneously in biomolecular condensates formed by scaffolds and surfactant clients. *Sci. Rep.* **11** (2021), doi:10.1038/s41598-021-94309-y.

25. A. Wiącek, E. Chibowski, Zeta potential, effective diameter and multimodal size distribution in oil/water emulsion. *Colloids Surfaces A Physicochem. Eng. Asp.* **159**, 253–261 (1999).

26. A. Avranas, G. Stalidis, G. Ritzoulis, Demulsification rate and zeta potential of O/W emulsions. *Colloid Polym. Sci.* **266**, 937–940 (1988).

27. B. Salopek, D. Krasic, S. Filipovic, Measurement and application of zeta-potential. *Rud. Zb.* **4**, 147–151 (1992).

28. P. Atkins, J. De Paula, J. Keeler, *Atkin's Physical Chemistry, 11th Ed* (2017).

29. W. B. Russel, D. A. Saville, W. R. Schowalter, *Colloidal Dispersions* (Cambridge University Press, Cambridge, 1989; https://www.cambridge.org/core/books/colloidal-dispersions/A880F349E6ECA53C2E65D0FDEDABB091).

30. J. N. Losso, A. Khachatryan, M. Ogawa, J. S. Godber, F. Shih, Random centroid optimization of phosphatidylglycerol stabilized lutein-enriched oil-in-water emulsions at acidic pH. *Food Chem.* **92**, 737–744 (2005).

31. S. Gurung, M. Holzer, S. Barnert, R. Schubert, Preparation and characterization of phospholipid stabilized nanoemulsions in small-scale. *bioRxiv* (2019), submission date: April 09, 2019, asscessed: May 25, 2021 doi:10.1101/603803.

32. I. Ostolska, M. Wiśniewska, Application of the zeta potential measurements to explanation of

colloidal Cr(2)O(3) stability mechanism in the presence of the ionic polyamino acids. *Colloid Polym. Sci.* **292**, 2453–2464 (2014).

33. I. K. Hong, S. I. Kim, S. B. Lee, Effects of HLB value on oil-in-water emulsions: Droplet size, rheological behavior, zeta-potential, and creaming index. *J. Ind. Eng. Chem.* **67**, 123–131 (2018).

34. K. L. Saar, Y. Zhang, T. Müller, C. P. Kumar, S. Devenish, A. Lynn, U. Łapińska, X. Yang, S. Linse, T. P. J. Knowles, On-chip label-free protein analysis with downstream electrodes for direct removal of electrolysis products. *Lab Chip*. **18**, 162–170 (2018).

35. K. L. Saar, T. Muller, J. Charmet, P. K. Challa, T. P. J. Knowles, Enhancing the Resolution of Micro Free Flow Electrophoresis through Spatially Controlled Sample Injection. *Anal. Chem.* **90**, 8998–9005 (2018).

36. W. E. Arter, J. Charmet, J. Kong, K. L. Saar, T. W. Herling, T. Müller, U. F. Keyser, T. P. J. Knowles, Combining Affinity Selection and Specific Ion Mobility for Microchip Protein Sensing. *Anal. Chem.* **90**, 10302–10310 (2018).

37. B. D. Freibaum, J. P. Taylor, The Role of Dipeptide Repeats in C9ORF72-Related ALS-FTD. *Front. Mol. Neurosci.* **10**, 1–9 (2017).

38. S. Boeynaems, E. Bogaert, D. Kovacs, A. Konijnenberg, E. Timmerman, A. Volkov, M. Guharoy, M. De Decker, T. Jaspers, V. H. Ryan, A. M. Janke, P. Baatsen, T. Vercruysse, R.-M. Kolaitis, D. Daelemans, J. P. Taylor, N. Kedersha, P. Anderson, F. Impens, F. Sobott, J. Schymkowitz, F. Rousseau, N. L. Fawzi, W. Robberecht, P. Van Damme, P. Tompa, L. Van Den Bosch, Phase Separation of C9orf72 Dipeptide Repeats Perturbs Stress Granule Dynamics. *Mol. Cell*. **65**, 1044-1055.e5 (2017).

39. H. Baechtold, M. Kuroda, J. Sok, D. Ron, B. S. Lopez, A. T. Akhmedov, Human 75-kDa DNA-pairing protein is identical to the pro-oncoprotein TLS/FUS and is able to promote D-loop formation. *J. Biol. Chem.* **274**, 34337–34342 (1999).

40. N. E Farrawell, I. Lambert-Smith, S. Warraich, I. P Blair, D. Saunders, D. M Hatters, J. Yerbury, Distinct partitioning of ALS associated TDP-43, FUS and SOD1 mutants into cellular inclusions. *Sci. Rep.* **5**, 13416 (2015).

41. A. D. Efimova, R. K. Ovchinnikov, A. Y. Roman, A. V. Maltsev, V. V. Grigoriev, E. A. Kovrazhkina, V. I. Skvortsova, The FUS protein: Physiological functions and a role in

amyotrophic lateral sclerosis. *Mol. Biol.* **51**, 341–351 (2017).

42. A. C. Murthy, G. L. Dignon, Y. Kan, G. H. Zerze, S. H. Parekh, J. Mittal, N. L. Fawzi, Molecular interactions underlying liquid−liquid phase separation of the FUS low-complexity domain. *Nat. Struct. Mol. Biol.* **26**, 637–648 (2019).

43. J. T. Overbeek, M. J. Voorn, Phase separation in polyelectrolyte solutions; theory of complex coacervation. *J Cell Physiol Suppl*. **49**, 7–22 (1957).

44. L. M. Jawerth, M. Ijavi, M. Ruer, S. Saha, M. Jahnel, A. A. Hyman, F. Jülicher, E. Fischer-Friedrich, Salt-Dependent Rheology and Surface Tension of Protein Condensates Using Optical Traps. *Phys. Rev. Lett.* **121**, 258101 (2018).

45. A. R. Tejedor, A. Garaizar, J. Ramírez, J. R. Espinosa, 'RNA modulation of transport properties and stability in phase-separated condensates. *Biophys. J.* **120**, 5169–5186 (2021).

46. S. Das, Y. H. Lin, R. M. Vernon, J. D. Forman-Kay, H. S. Chan, Comparative roles of charge, π, and hydrophobic interactions in sequence-dependent phase separation of intrinsically disordered proteins. *Proc. Natl. Acad. Sci. U. S. A.* **117** (2020), doi:10.1073/pnas.2008122117.

47. G. L. Dignon, W. Zheng, Y. C. Kim, R. B. Best, J. Mittal, Sequence determinants of protein phase behavior from a coarse-grained model. *PLoS Comput. Biol.* **14**, e1005941 (2018).

48. R. García Fernández, J. L. F. Abascal, C. Vega, The melting point of ice Ih for common water models calculated from direct coexistence of the solid-liquid interface. *J. Chem. Phys.* **124**, 144506 (2006).

49. A. J. C. Ladd, L. V. Woodcock, Triple-point coexistence properties of the lennard-jones system. *Chem. Phys. Lett.* **51**, 155–159 (1977).

50. J. R. Espinosa, E. Sanz, C. Valeriani, C. Vega, On fluid-solid direct coexistence simulations: The pseudo-hard sphere model. *J. Chem. Phys.* **139**, 144502 (2013).

51. D. A. Case, T. E. Cheatham, T. Darden, H. Gohlke, R. Luo, K. M. Merz, A. Onufriev, C. Simmerling, B. Wang, R. J. Woods, The Amber biomolecular simulation programs. *J. Comput. Chem.* **26**, 1668–1688 (2005).

52. L. Monticelli, S. K. Kandasamy, X. Periole, R. G. Larson, D. P. Tieleman, S. J. Marrink, The MARTINI coarse-grained force field: Extension to proteins. *J. Chem. Theory Comput.* **4**, 819–

834 (2008).

53. S. O. Yesylevskyy, L. V. Schäfer, D. Sengupta, S. J. Marrink, Polarizable water model for the coarse-grained MARTINI force field. *PLoS Comput. Biol.* **6**, 1–17 (2010).

54. T. A. Wassenaar, K. Pluhackova, R. A. Böckmann, S. J. Marrink, D. P. Tieleman, Going backward: A flexible geometric approach to reverse transformation from coarse grained to atomistic models. *J. Chem. Theory Comput.* **10**, 676–690 (2014).

55. A. F. Harrison, J. Shorter, RNA-binding proteins with prion-like domains in health and disease. *Biochem. J.* **474** (2017), pp. 1417–1438.

56. J. Kang, L. Lim, Y. Lu, J. Song, A unified mechanism for LLPS of ALS/FTLD-causing FUS as well as its modulation by ATP and oligonucleic acids. *PLOS Biol.* **17**, e3000327 (2019).

57. Z. Sun, Z. Diaz, X. Fang, M. P. Hart, A. Chesi, J. Shorter, A. D. Gitler, Molecular Determinants and Genetic Modifiers of Aggregation and Toxicity for the ALS Disease Protein FUS/TLS. *PLoS Biol.* **9**, e1000614 (2011).

58. S. Qamar, G. Z. Wang, S. J. Randle, F. S. Ruggeri, J. A. Varela, J. Q. Lin, E. C. Phillips, A. Miyashita, D. Williams, F. Ströhl, W. Meadows, R. Ferry, V. J. Dardov, G. G. Tartaglia, L. A. Farrer, G. S. Kaminski Schierle, C. F. Kaminski, C. E. Holt, P. E. Fraser, G. Schmitt-Ulms, D. Klenerman, T. Knowles, M. Vendruscolo, P. St George-Hyslop, FUS Phase Separation Is Modulated by a Molecular Chaperone and Methylation of Arginine Cation-π Interactions. *Cell*. **173**, 720--734.e15 (2018).

59. S. Cuylen, C. Blaukopf, A. Z. Politi, T. Muller-Reichert, B. Neumann, I. Poser, J. Ellenberg, A. A. Hyman, D. W. Gerlich, Ki-67 acts as a biological surfactant to disperse mitotic chromosomes. *Nature*. **535** (2016), doi:10.1038/nature18610.

60. T. Lu, E. Spruijt, Multiphase Complex Coacervate Droplets. *J. Am. Chem. Soc.* **142** (2020), doi:10.1021/jacs.9b11468.

61. J. Yoo, A. Aksimentiev, The structure and intermolecular forces of DNA condensates. *Nucleic Acids Res.* **44**, 2036–2046 (2016).

62. R. Evans, The role of capillary wave fluctuations in determining the liquid-vapour interface analysis of the van der waals model. *Mol. Phys.* **42**, 1169–1196 (1981).

63. J. Benet, L. G. Macdowell, E. Sanz, Computer simulation study of surface wave dynamics at the crystal-melt interface. *J. Chem. Phys.* **141**, 034701 (2014).

64. J. R. Espinosa, J. A. Joseph, I. Sanchez-Burgos, A. Garaizar, D. Frenkel, R. Collepardo-Guevara, Liquid network connectivity regulates the stability and composition of biomolecular condensates with many components. *Proc. Natl. Acad. Sci. U. S. A.* **117**, 13238–13247 (2020).

65. D. Zwicker, R. Seyboldt, C. A. Weber, A. A. Hyman, F. Jülicher, Growth and division of active droplets provides a model for protocells. *Nat. Phys.* **13** (2017), doi:10.1038/nphys3984.

66. D. Zwicker, A. A. Hyman, F. Jülicher, Suppression of Ostwald ripening in active emulsions. *Phys. Rev. E - Stat. Nonlinear, Soft Matter Phys.* **92**, 012317 (2015).

67. W. M. Babinchak, R. Haider, B. K. Dumm, P. Sarkar, K. Surewicz, J.-K. Choi, W. K. Surewicz, The role of liquid-liquid phase separation in aggregation of the TDP-43 low complexity domain. *J. Biol. Chem.* **294**, 6306–6317 (2019).

68. Y. Lin, D. S. W. Protter, M. K. Rosen, R. Parker, Formation and Maturation of Phase-Separated Liquid Droplets by RNA-Binding Proteins. *Mol. Cell*. **60**, 208–219 (2015).

69. C. Weber, T. Michaels, L. Mahadevan, Spatial control of irreversible protein aggregation. *Elife*. **8**, e42315 (2019).

70. M. Garcia-Jove Navarro, S. Kashida, R. Chouaib, S. Souquere, G. Pierron, D. Weil, Z. Gueroui, RNA is a critical element for the sizing and the composition of phase-separated RNA–protein condensates. *Nat. Commun.* **10**, 3230 (2019).

71. S. Uppaluri, S. C. Weber, C. P. Brangwynne, Hierarchical Size Scaling during Multicellular Growth and Development. *Cell Rep.* **17**, 345–352 (2016).

72. M. Derenzini, D. Trerè, A. Pession, M. Govoni, V. Sirri, P. Chieco, Nucleolar size indicates the rapidity of cell proliferation in cancer tissues. *J. Pathol.* **191**, 181–186 (2000).

TOC graphic

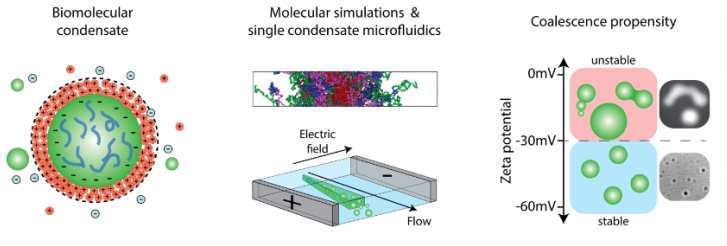
Biomolecular condensate
Molecular simulations & single condensate microfluidics
Electric field
Flow
Coalescence propensity
Zeta potential
0mV
-30mV
-60mV
unstable
stable